Enhanced Ocean Wave Modeling by Including Effect of Breaking under Both Deep- and Shallow-Water Conditions

Yue Xu[1] and Xiping Yu[2]

[1] Department of Hydraulic Engineering, Tsinghua University, Beijing, China.

[2] Department of Ocean Science and Engineering, Sothern University of Science and Technology, Shenzhen, China.

Correspondence to: Xiping Yu (yuxp@sustech.edu.cn)

10   **Abstract**

11   Accurate description of the wind energy input into ocean waves is crucial to ocean

12 wave modeling and a physics-based consideration on the effect of wave breaking is

13 absolutely necessary to obtain such an accurate description. This study evaluates the

14 performance of an improved formula recently proposed by Xu and Yu (2020), who took into

15 account not only the effect of breaking but also the effect of air-flow separation on the

16 leeside of steep wave crests in a reasonably consistent way. Numerical results are obtained

17 through coupling an enhanced atmospheric wave boundary layer model with the ocean wave

18 model WaveWatch III (v5.16). The coupled model has been extended to be valid in both

19 deep and shallow waters. Duration-limited waves under controlled normal conditions and

20 storm waves under practical hurricane conditions are studied in details to verify the

21 improved model. Both the representative wave parameters and the parameters characterizing

22 the wave spectrum are discussed. It is shown that the improved source-term package for the

23 wind energy input and the wave energy dissipation leads to more accurate results under all

24 conditions. It performs evidently better than other standard source-term options of ST2, ST4

25 and ST6 embedded in WaveWatch III. It is also demonstrated that the improvement is

26 particularly important for waves at their early development stage and waves in shallow

27 waters.

28 **Keywords**: Source-term option; Breaking effect; Atmospheric wave boundary layer model;

29 WaveWatch III; Duration-limited waves; Hurricane-generated waves.

1. Introduction

Accurate modeling of ocean waves depends straightforwardly on a correct formulation of the wind energy supply to the waves through the ocean surface as well as the wave energy dissipation within the ocean surface layer, and eventually on a thorough understanding to the physics underlying these two dynamic processes. The wind energy input supports the generation and growth of ocean waves, while the wave energy dissipation always occurs owing not only to the viscous property of the fluid but also to the effects of turbulent mixing and multiphase interaction that take place in the boundary layer at both sides of the air-sea interface. In the past decades, a tremendous number of research efforts have been made to enhance our understanding on the phenomena of wind energy input into ocean waves and the dissipation of ocean surface waves due to various mechanisms. However, a comprehensive integration of the accumulated knowledge, particularly those developed under extreme conditions in shallow waters, does not seem to have been satisfactorily achieved up to date.

Janssen (1989; 1991; 2004) proposed the most classical formula for the wind energy input based on the resonance theory of Miles (1957; 1965), in which the wind drag as a deterministic function of the roughness height of the ocean surface is a critical parameter. Hasselmann et al. (1973) obtained an expression for the wind energy input by solving the wave energy equation and then calibrating parameters with field data from the joint North Sea wave project (JONSWAP). Snyder et al. (1981) and Donelan et al. (2006) conducted field experiments in the Bight of Abaca, Bahamas, and Lake George, Australia, and included more physics in their formula for the wind energy input. Badulin et al. (2007) and Zakharov et al. (2012; 2017) proposed a new method to establish a theory for the wind energy input by considering the weakly turbulent law for wind-wave growth. In spite of these important achievements, the wind energy input is still not yet satisfactorily formulated, basically due to complexity of the phenomenon as well as the physics underlying the phenomenon.

Researchers have found substantial differences between wind energy input through ocean surfaces with and without wave breaking (Banner and Melville, 1976). Data collected during the AUSWEX field campaign at Lake George, Australia (Babanin et al., 2007)

59 showed that under a severe breaking condition, the wind energy input will increase to about

60 2 times of that under a relevant non-breaking condition. Although the important effects of

61 wave breaking as well as short-wave dissipation on wind energy input have been well

62 understood (Janssen, 1989, 1991; Makin and Kudryavtsev, 1999; Hasselmann et al., 1973;

63 Babanin et al., 2007), it is only until recent that Xu and Yu (2020) proposed a formula to

64 effectively include these effects. Xu and Yu (2020)'s formula takes into consideration both

65 the breaking effect and the effect of air-flow separation on the leeside of steep wave crests

66 in a reasonably consistent way. Despite of its physics-based nature, a further evaluation of

67 its performance in practical and more complicated wind wave conditions, however, is still

68 necessary.

69   It is generally believed that, among the total wind energy transferred into the ocean

70 waves, a part is absorbed by the long-wave components to support wave growth while an

71 even larger part is received by the short-wave components and quickly dissipated due to

72 fluid viscosity, wind shear on the ocean surface and the turbulence effect related to wave

73 breaking (Csanady, 2001; Jones and Toba, 2001). Formulation of the wave dissipation,

74 however, is very difficult and the available suggestions in the literature are rather

75 controversial (Cavaleri et al., 2007). The earliest wave dissipation model is known to be the

76 probabilistic breaking model originally presented by Longuet-Higgins (1969) and then

77 improved by Yuan et al. (1986). Hasselmann (1974) proposed the whitecap model based on

78 a mathematical formulation of the negative work done by the downward whitecap pressure

79 on the upward wave motion. Phillips (1985) and Donelan and Pierson (1987) proposed the

80 quasi-saturation model by assuming a local equilibrium relationship among wind energy

81 input, nonlinear transfer and wave dissipation. Polnikov (1993) preferred the turbulence

82 dissipation model which relates the loss of wave energy to the dissipation of turbulence

83 kinetic energy. In addition to the theoretical studies, a significant number of experimental

84 investigations have also been carried out (Phillips et al., 2001; Melville and Matusov, 2002;

85 Donelan, 2001; Hwang, 2005). Based on the data measured at Lake George, Australia,

86 Bananin and Young (2005) established an empirical model, in which the concept of

87 cumulative effect is introduced so that the contribution of low-frequency wave motion to

88   breaking of high-frequency waves can be taken into account. It may be necessary to point

89   out that most of the experimental studies are supported only by limited data.

90   WaveWatch III (WWIII), a successful third-generation wave model, has been widely

91   used for simulating ocean waves in both deep and shallow waters. With great efforts made

92   by scientists around the world (Ardhuin et al., 2010; Zieger et al., 2015), parameterizations

93   of the source terms in WWIII have been well calibrated under various conditions to achieve

94   satisfactory results for evolution of an ocean wave spectrum. Under severe wave conditions,

95   however, their accuracy is often unsatisfactory and the wave energy is underestimated even

96   with an optimal choice of the parameters (Cavaleri et al., 2020; Campos et al., 2018;

97   Mentaschi et al., 2015). Meanwhile, researchers found that the directional wave spectrum

98   has been sometimes very poorly simulated even when the significant wave parameters are

99   accurately represented (Fan and Rogers, 2016). Stopa et al. (2016) believed that all wave

100   models have difficulty in describing the directional spread of waves. Although modelers

101   usually tend to attribute the numerical error to the inaccuracy of the wind data or topography

102   data, we must admit that imperfection of the source term parameterization, especially under

103   severe wave conditions, is also one of the main reasons.

104   In this study, improved formulas for the wind energy input and the wave energy

105   dissipation are embedded into the WWIII version 5.16, though it may also be applied to

106   other ocean wave models. The enhanced atmospheric wave boundary layer model (AWBLM)

107   (Xu and Yu, 2021) is also coupled to ensure a more accurate wind stress evaluation at high

108   wind speed and in finite water depth. The performances of the improved formulas are

109   evaluated under both idealized wind conditions and real extreme conditions. Attention is

110   also paid to their differences in deep- and shallow-waters. The structure of the paper is

111   arranged as follows. The improved formulation as well as the framework of the coupled

112   AWBLM-WWIII model are described in Section 2. Model verification under controlled

113   conditions is presented in Section 3, while model verification under extreme wind

114   conditions is presented in Section 4. Section 5 is a summary of conclusions.

2. Model Description

2.1 Coupled AWBLM-WWIII Model

The ocean wave model WaveWatch III numerically solves the energy conservation equation for wave action density spectrum (WW3DG, 2016):

$$\frac{DN}{Dt} = \frac{S}{\omega} \tag{1}$$

$$S = S_{in} + S_{ds} + S_{nl} \tag{2}$$

where $N(\omega,\theta)$ is the wave action density spectrum; ω is the relative frequency; S is the source/sink term given by Eq. (2). In general, the source term S must represent three different mechanisms: the wind energy input into waves S_{in}, the wave energy dissipation S_{ds}, the nonlinear wave-wave interaction S_{nl}. Although S_{in} and S_{ds} represent different physical processes, they should be considered and calibrated interrelatedly since the net effect of these two sources rather than each of them can be more accurately measured on many occasions and it is the net effect that governs the growth/decay of the ocean waves. S_{nl} plays a key role in the evolution of wave spectrum shape and may, at least theoretically, be evaluated through correctly solving the nonlinear transfer integrals. Note that, in shallow waters, the wave energy dissipation must include those due to bottom friction and depth-induced breaking, denoted by S_{dsf} and S_{dsb}, respectively, in addition to that due to whitecaps, denoted by S_{dsw}, i.e., $S_{ds} = S_{dsf} + S_{dsb} + S_{dsw}$. It may also be worthwhile mentioning that an accurate evaluation of the nonlinear interaction effect is surprisingly difficult for the high-frequency wave components, particularly in shallow waters. Therefore, it is frequently suggested to apply a semi-empirical theory for evaluating S_{nl}, i.e., let $S_{nl} = S_{nl4} + S_{nl3}$, where S_{nl4} and S_{nl3} are expressed as functions of the wave frequency as well as the wave direction, and represent the quartet and triad wave interactions, which play dominant roles in deep and shallow waters, respectively.

In order to accurately simulate ocean waves under moderate to severe wind conditions, and from deep to shallow water conditions, an advanced atmospheric wave boundary layer model (AWBLM) must be coupled into WWIII for a dynamic evaluation of the wind stress.

142   The AWBLM applicable for this purpose is well described in Xu and Yu (2021), which may

143   take effects of both ocean surface state and water depth into consideration, and has certain

144   advantages compared to a simple quadratic formula for the wind stress. In the coupled

145   model, the source terms are treated in the following way. Quartet-wave interaction is

146   computed with the standard discrete interaction approximation (DIA). Note that, though it

147   may bring some uncertainty into the numerical results for nonlinear effects, the DIA method

148   is still widely employed in practical applications due to its minimum requirement on the

149   computational efforts (Liu et al., 2017; Stopa et al., 2015; Ardhuin et al., 2010). Triad-wave

150   interaction is evaluated with the Lumped Triad Approximation model (Eldeberky, 1996).

151   The bottom friction effect is described by the simple model of JONSWAP (Hasselmann et

152   al., 1973). The Battjes and Janssen (1978) parameterization is employed to represent the

153   effect of depth-induced breaking. The parameters included in all source terms except for

154   those with special emphases follow the default setting. The wind energy input and the wave

155   energy dissipation are considered as a package in this study. WWIII provides four typical

156   options of this package, i.e., ST2, ST3, ST4, ST6, among which ST3 and ST4 are based on

157   the same formulation of Janssen (2004) for the wind energy input. Since ST4 has been

158   frequently reported to have a better performance than ST3 (Stopa et al., 2016; Beyá et al.,

159   2017; Liu et al., 2017), the ST3 option is neglected in this study. The standard options are

160   carefully compared with the improved model proposed by the present authors (Xu and Yu,

161   2020).

2.2 Improved Model of Xu and Yu (2020)

163   The wind energy input in the improved model of Xu and Yu (2020), hereafter referred as

164   ST-XY option, is expressed by

$$S_{\text{in}}\left(k,\theta\right) = \frac{\rho_{\text{a}}}{\rho_{\text{w}}} \omega \gamma_{\text{g}}\left(k,\theta\right) E\left(k,\theta\right) \tag{3}$$

$$\gamma_{\text{g}}\left(k,\theta\right) = a\left[b_{\text{T}}\lambda G' + \left(1 - b_{\text{T}}\right)G\right]W^2 \sqrt{B_{\text{n}}} \tag{4}$$

$$W = \max\left(0, \frac{U_{10}}{c_{\text{p}}}\cos\left(\theta - \theta_{\text{a}}\right) - 1\right) + a_0 \min\left(0, \frac{U_{10}}{c_{\text{p}}}\cos\left(\theta - \theta_{\text{a}}\right) - 1\right) \tag{5}$$

168
$$B_\mathrm{n}\left(k\right) = A\left(k\right)\int_0^{2\pi} k^3 E\left(k,\theta'\right)d\theta' \tag{6}$$

169
$$b_\mathrm{T}\left(k\right) = 89.5\left(\sqrt{B_\mathrm{n}\left(k\right)} - 0.0223\right)^2 \tag{7}$$

170
$$G = 2.8 - 1.0\left\{1 + \tanh\left[10\sqrt{B_\mathrm{n}}\left(\frac{U_{10}}{c_\mathrm{p}}\cos\left(\theta - \theta_\mathrm{a}\right) - 1\right)^2 - 11\right]\right\} \tag{8}$$

171   where ρ_a is the density of air; ρ_w is the density of water; ω is radian frequency; k is

172   the wavenumber, which is related to ω through the dispersion relation; θ is the wave

173   direction; $E\left(k,\theta\right)$ is the directional wave energy spectrum; $\gamma_\mathrm{g}\left(k,\theta\right)$ is the wave growth

174   rate; c_p is the celerity of the wave with peak frequency; U_{10} is the wind speed at the 10 m

175   level above the ocean surface; θ_a is the wind directon. Note that the basic form of Eq. (3)

176   follows the conventional assumption that S_in is propotional to the directional wave

177   spectrum. However, the most crucial factor in S_in, i.e., the wave growth rate γ_g is

178   formulated to represent the effect of various physical processes. Although γ_g is essentially

179   governed by the relative wind speed and the mean steepness of the surface waves, it is

180   considered to be essentially different when wave breaking does or does not occur, and is

181   thus expressed as a weighted average of the different multipliers corresponding to breaking

182   and non-breaking conditions with the breaking probability b_T being the weight. The

183   relative wind speed is expressed by Eq. (5), where deflection of the wind direction from the

184   wave direction is fully considered. It may be necessary to point out that the contribution of

185   the inverse wind to energy input is reduced by a factor of $a_0 = 0.45$ following Liu et al.

186   (2017). Under the non-breaking condition, a separation coefficient G is introduced to

187   represent the 'shelter effect' due to airflow seperation at the lee side of high wave crests

188   following Donelan et al. (2006). When wave breaks, the 'shelter effect' disappears and G

189   reduces to its maximum value $G' = 2.8$. Since wave breaking has an effect of intensifying

190   wind energy input, we introduce an amplification factor λ, and let $\lambda = 2.0$, also

191   following previous studies. It may also be necessary to mention that the wave steepness is

192   related to the satuarated wave spectrum $B_\mathrm{n}\left(k\right)$, as expressed by Eq. (6), where $A\left(k\right)$ is a

193   measure of the directional spectrum width. In general, the wind energy input is positive, but

194   it may become negative when a strong swell is in presence and the wind speed is smaller

195   than the wave celerity or when the direction of wind is significantly deflected from the wave

196   direction.

197   The advantage of the wind energy input in the improved model of Xu and Yu (2020) is

198   its direct representation of the underlying physics. Based on the field observations of both

199   Donelan et al. (2006) and Babanin et al. (2007), the wind energy input into waves under

200   severe conditions is a very complicated process, since random waves may break and may

201   not break depending on the instantaneous local wave steepness. For non-breaking waves,

202   air-flow separation occurs on the leeside of wave crests, and the wind energy input reduces.

203   For breaking waves, the wind energy input is significantly larger due to breaking induced

204   mixing. The improved model of Xu and Yu (2020) fully considers these two effects and,

205   consequently, should be more suitable for the description of severe waves.

206   Since the ocean wave development depends actually on the net energy gain in the ocean

207   surface layer and it is sometimes very difficult to identify if some amount of wind energy is

208   transferred into the ocean waves and then dissipated or it is dissipated within the

209   atmospheric boundary layer and not received by the ocean at all, S_{in} and S_{ds} must then

210   be considered as a package. In other words, formulation of the dissipation term should be

211   based on a relevant definition of the wind energy input. In this study, we follow the wave

212   dissipation model of Ardhuin et al. (2010) for the whitecap effect. The semi-empirical

213   dissipation model of Ardhuin et al. (2010) can be expressed as (see also Leckler et al., 2013)

214
$$S_{dsw} = S_{dsn} + S_{dsc} \tag{9}$$

215
$$S_{dsn} = \xi_n B_r^{-2} \omega \left\{ \delta_d \max\left[B(k) - B_r, 0 \right]^2 + (1 - \delta_d) \max\left[B'(k,\theta) - B_r, 0 \right]^2 \right\} E(k,\theta) \tag{10}$$

216
$$S_{dsc} = -1.44 \xi_c \left\{ \int_0^{r_c k} \int_0^{2\pi} \max\left[\sqrt{B(k',\theta')} - \sqrt{B_r}, 0 \right]^2 \Delta c_p d\theta' dk' \right\} E(k,\theta) \tag{11}$$

217   where, ξ_n and ξ_c are empirical constants; δ_d is a factor introduced to weight the

218   isotropic part and direction-dependent part; r_c is the minimum ratio of the wavenumber

219   that will wipe out the short waves. The saturation spectrum $B_{\mathrm{n}}(k)$ is defined in the same

220   way as before and the directional saturation spectrum $B_{\mathrm{n}}'(k,\theta)$ is defined by

221
$$B'(k,\theta) = \int_{\theta-\Delta_{\theta}}^{\theta+\Delta_{\theta}} k^3 \cos^2(\theta-\theta') E(k,\theta') d\theta' \qquad (12)$$

222   The threshold of $B_{\mathrm{n}}(k)$ is denoted by B_{r}. Note that Eqs. (9), (10) and (11) are based the

223   assumption that wave dissipation consists of an inherent effect and a cumulative effect, both

224   are propotional to the directional wave spectrum. In shallow waters, dissipations due to

225   bottom friction and depth-induced breaking are formulated following Xu and Yu (2021).

226   **2.3 Standard Models**

227   Known reliable formulas for the wind energy input and the wave energy dissipation

228   have been embedded in WWIII. Among all, the following options, which have been widely

229   preferred on different occasions, are chosen for comparison in this study.

230   **(1) ST2 option.** This package, originally proposed by Tolman and Chalikov (1996),

231   consists of the wind energy input formula of Chalikov and Belevich (1993) and Chalikov

232   (1995) as well as a relevant wave energy dissipation model. The dissipation model

233   emphasizes the different mechanisms of dissipation for low- and high-frequency waves. The

234   expression for low-frequency waves is based on an analogy to energy dissipation due to

235   turbulence, while that for high-frequency waves is purely empirical. A linear combination of

236   these two expressions then represents the total dissipation. It has been reported that this

237   wind energy input formula may need to be filtered using a special technique when a strong

238   swell is in presence (Tolman, 2002). For the purpose of comparison, the default setting of

239   parameters in this study follows Tolman (2002), who selected this package in WWIII for a

240   global ocean wave modeling and obtained satisfactory results.

241   **(2) ST4 option.** This package consists of the wind energy input formula of Janssen

242   (2004), which is based on the wave growth theory of Miles (1957), and the wave energy

243   dissipation model of Ardhuin et al. (2010). The dissipation model appears as the summation

244   of an inherent part and a cumulative part. All parameters are determined following Ardhuin

245   et al. (2010).

246   **(3) ST6 option.** This package consists of the formulas for wind energy input and wave

247   energy dissipation due to whitecaps which fit the field data obtained at Lake George,

248   Australia (Donelan et al., 2006; Rogers et al., 2012). A sink term due to negative wind

249   energy input is considered for inverse winds. The dissipation due to whitecaps is expressed

250   as the sum of an inherent part, which is proportional to wave spectrum, and a cumulative

251   part in terms of the integral properties of the wave spectrum below a certain value of the

252   wavenumber.

3. Model Verification under Controlled Normal Conditions

3.1 Duration-limited waves in deep waters

255   The ideal problem of wave development over the open sea of infinite water depth is

256   considered. At a given duration, evolution of the directional wave spectrum is simulated

257   with WWIII considering different choices of the source-term package. The uniform wind

258   speed at the 10 m height above ocean surface is fixed at a moderate level of 10 m/s.

259   Sensitivity of the numerical results to the computational time step is also studied. It is

260   shown that little difference of the numerical results can be observed as the computational

261   time step takes 30 s, 1 min and 10 min. Therefore, the results obtained with the time step

262   equal to 10 min are presented in the remaining part of this study.

263   In Figure 1, the wave growth curve, i.e., the relationship between the normalized total

264   wave energy ε and the normalized duration τ, computed with different options for the

265   source terms, is presented and compared with the empirical results available in the literature.

266   The four empirical growth curves correspond to Stewart's (1961) law, which was originally

267   presented as tabulated data, Sanders' (1976) law, the CERC (1977) law and Kahma and

268   Calkoen's (1992) law. The equilibrium value given by the Pierson-Moskowitz spectrum

269   (Pierson and Moskowitz, 1964), i.e., $\varepsilon_{PM} = 3.6 \times 10^{-3}$, as well as the tabulated values of

270   Moskowitz (1964) are also plotted.

271
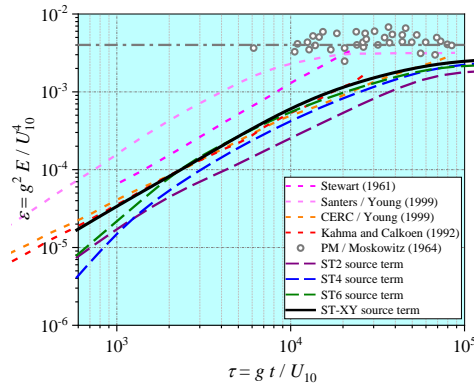
Figure 1. Comparisons of duration-limited growth rate between empirical and computational
results. Both wave energy and duration are nondimensionalized with U_{10}

274   By comparing the computed wave growth curves with each other and with the empirical

275   results as well, it becomes clear that, the WWIII model results with different choices of the

276   source-term package are all rather close to the CERC (1977) law and Kahma and Calkoen's

277   (1992) law, and also agree with the results of Rogers et al. (2012). At a younger wave age,

278   particularly at $\tau < 2 \times 10^3$, the ST-XY option performs much better while other

279   source-term options underestimate the wave energy significantly. The ST4 option most

280   severely underestimate the wave energy at the early stage of wave development. As duration

281   increases, the results of the ST6 option approaches those of the ST-XY option. When

282   approaching the equilibrium stage ($10^4 < \tau < 10^5$), the numerical results corresponding to

283   ST-XY, ST6 and ST4 options all approach the Pierson-Moskowitz limit while the ST2

284   option still underestimate the wave energy. In general, the performance of the ST-XY option

285   is obviously better.

286   Since the source terms are often formulated in terms of the mean wave parameters,

287   evolution of the wave spectrum and development of the mean wave parameters are thus

288   interdependent. Therefore, a comparison of the mean wave parameters obtained with

289   different choice of the source term options, as presented in Figure 2, is highly meaningful. It

290   is demonstrated that the significant wave height H_s and the mean wavelength L_m obtained

291   with the ST-XY option are slightly greater than the results obtained with other options while

292   the ST2 option yields the smallest values. The numerical result of the mean wave period T_{02}

293 obtained with the ST-XY option is the largest at the early wave development stage, but it

294 becomes almost the same as that obtained with the ST4 option at the equilibrium stage. The

295 mean wave period T_{02} obtained with the ST2 option is the smallest at the early

296 wave-development stage while that obtained with the ST6 option becomes smallest at the

297 equilibrium stage. The peak frequency f_p obtained with ST4, ST6 and ST-XY options is very

298 close to each other, but the ST2 option results in a larger value.
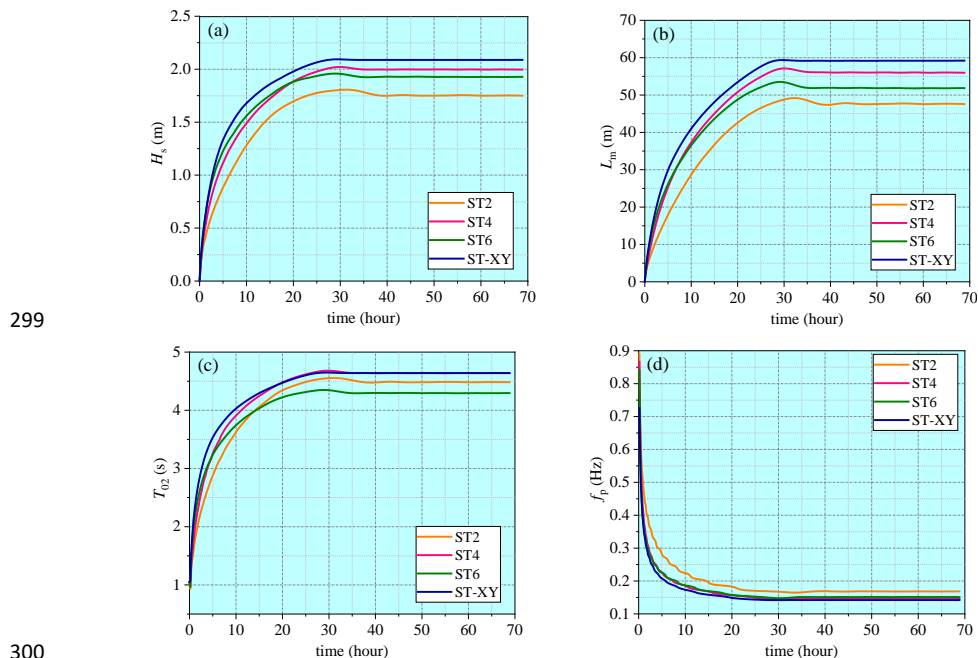
299
300

301 Figure 2. Comparisons of numerical results for (a) significant wave height H_s, (b) mean

302 wave length L_m, (c) mean wave period T_{02} and (d) peak frequency f_p, obtained with different

303 choices of the source-term options.

304   A comparison of the computed spectra of the wind energy input and the wave energy

305 dissipation with different choices of the source-term options is presented in Figure 3. Note

306 that the spectra obtained with the ST2 option are not presented since they are obviously

307 underestimated. The numerical results strongly indicate that the wind energy input and the

308 wave energy dissipation resulted from the same source-term package are correlated, not

309 only in terms of the peak values but also in terms of the spectral shapes. It is seen that, the

310 wind energy input resulted from the ST-XY option maintains at a higher level than those

311 resulted from other options at the early wave-development stage, leading to a faster wave

312 growth and higher level of the wave energy at younger wave ages. Relatively concentrated

313 unimodal distributions for both the wind energy input and the wave energy dissipation are

314 built at the early wave-development stage, no matter which source-term option is adopted.

315 As wave development continues, however, the peak frequencies as well as the peak values

316 of the spectra decrease while more wind energy is transferred to the higher frequency waves

317 and bimodal distributions are formed. At this stage, the peak value of the spectra obtained

318 with the ST-XY option is similar to those obtained with the ST6 and ST4 option, while its

319 high-frequency part has higher values than those resulted from the ST6 and ST4 options.

320 When approaching the fully-developed stage, the wind energy input obtained with the

321 ST-XY and ST4 options reaches a peak at relatively low frequency, but the peak obtained

322 with the ST6 option appears at a much higher frequency. This is related to whether the

323 breaking effect is fully considered when formulating the wind energy input.
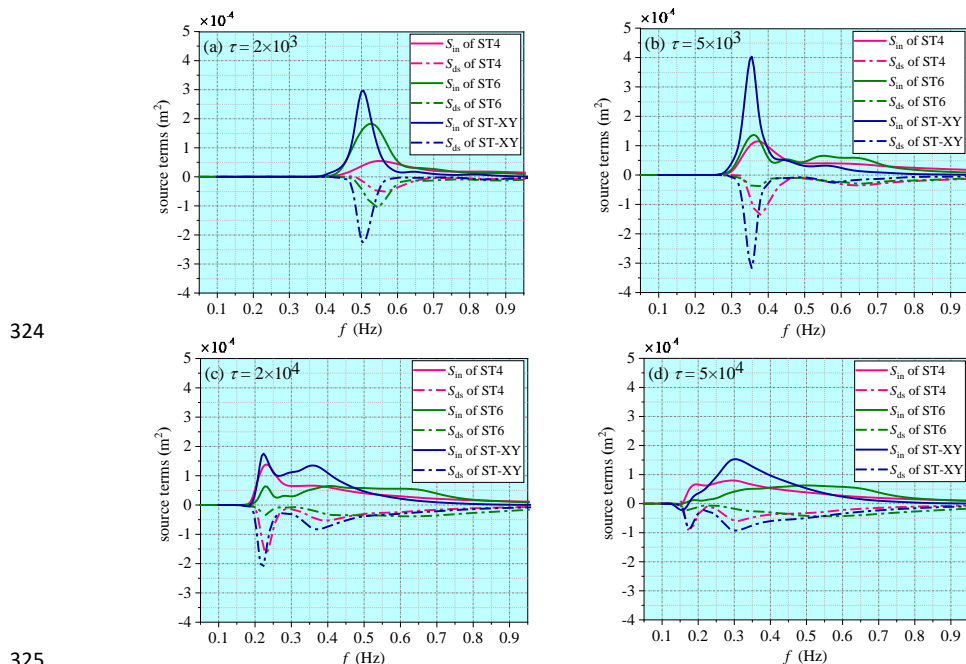
324

325

326 Figure 3. Spectra of the wind energy input and the wave energy dissipation obtained with

327 different choices of the source-term package.

328

329
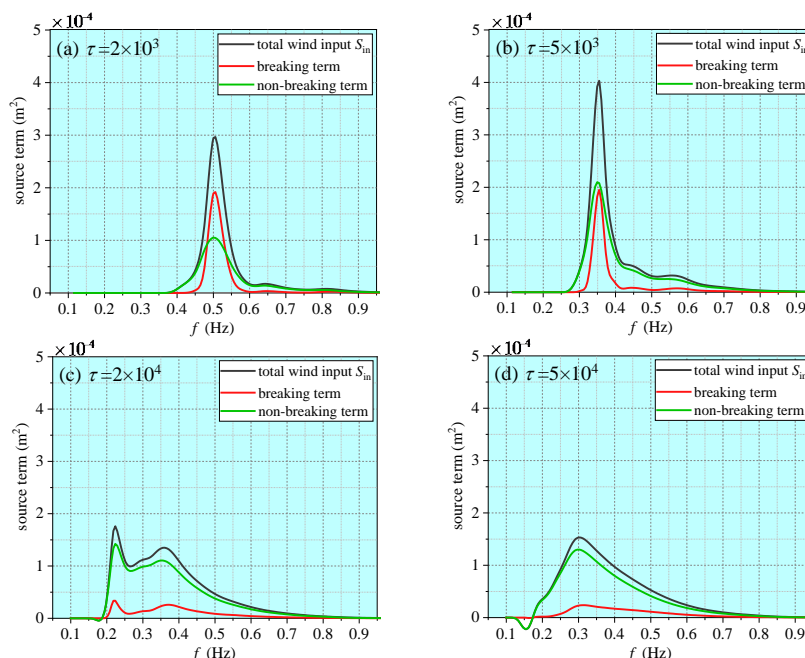
Figure 4. Deepwater spectra of wind energy input under breaking and non-breaking
conditions at different wave development stages given by the ST-XY source-term option

A major merit of the improved formula for the wind energy input of Xu and Yu (2020)
is the inclusion of breaking effect and the effect of airflow separation on the leesides of
steep waves. Among the total wind energy input, the portions taking place under breaking
and non-breaking conditions, given by the improved formula of Xu and Yu (2020), are
presented in Figure 4. It is clearly demonstrated that, at the early wave-development stage,
over 60% of the peak wind energy input takes place under the breaking condition. As wave
development continues, the proportion of the peak wind energy input under breaking
conditions decreases rapidly. When approaching the equilibrium stage, only 15% of the peak
wind energy input happens under breaking conditions. The trend suggested by our
numerical results is in very good agreement with the facts reported in previous studies
(Janssen, 1989; Hasselmann et al., 1973). It is thus reasonable to conclude that the ST-XY
option for the wind energy input and the wave energy dissipation successfully integrated the
known information about the effect of breaking on the wind energy input and improved the
performance of the WWIII model, especially at the early wave-development stage when the

346   wave energy has often been underestimated.

3.2 Duration-limited waves in shallow waters

348   In order to evaluate its performance in nearshore environment, the ST-XY source-term

349   option is also applied to the simulation of duration-limited waves in shallow waters. The

350   computational conditions are the same as those adopted in the deep-water case except for a

351   varying water depth from 5 m to 1 m. The nondimensional water depth $\delta = gd/U_{10}^2$ then

352   varies from 0.5 to 0.1. The computational results are compared with field observations of

353   Young and Verhagen (1996), who systematically measured the variations of wave

354   parameters and wave spectrum in shallow waters. Since the measured data was provided in

355   a fetch-limited manner, the method of Hwang and Wang (2004) is used to transfer the

356   duration-limited numerical results to fetch-limited ones for comparison. As demonstrated in

357   Figure 5, the numerical results obtained with the ST-XY source-term option in shallow

358   waters match well with the field data. As the nondimensional water depth increases from 0.1

359   to 0.5, the wave energy increases while the peak frequency decreases. This is well explained

360   by the effect of water depth on wave steepness and wave height. Within each range of the

361   water depth, the field data basically fall into the relevant two curves resulted from the model.

362   This is particularly accurate for the wave energy. Therefore, it may be concluded that the

363   improved source-term option of Xu and Yu (2020) is also effective for ocean wave modeling

364   under shallow water conditions.
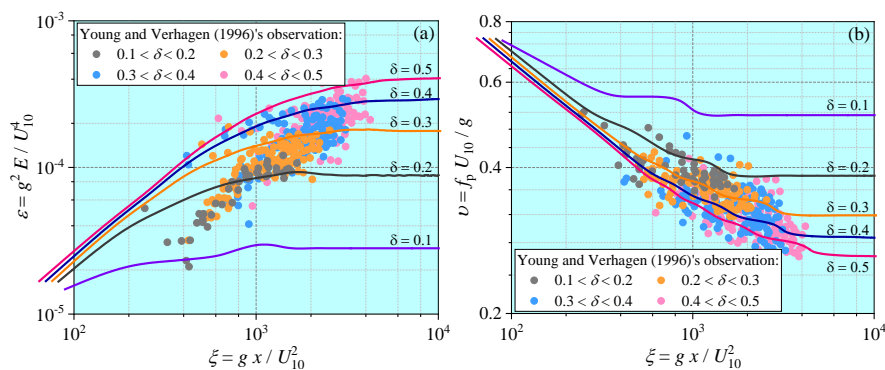
366   Figure 5. Comparisons of (a) fetch-limited growth rate and (b) wave age variation between

367   measured and computed results.

368   Intensified breaking is a major feature of the shallow water waves. Correct

369   representation of the breaking effect in the wind energy input is thus very important for

370   modeling shallow water waves. Different from the deep-water situation, the peak value of

371   the wind energy input taking place under breaking conditions are always higher than under

372   non-breaking conditions all through the early wave-development stage to the equilibrium

373   stage, as presented in Figure 6. The wind energy input taking place under breaking

374   conditions remains a high proportion even at the equilibrium stage, indicating a more

375   frequent breaking in shallow waters. In figure 7, the percentages of the wind energy input

376   taking place under breaking and non-breaking conditions at different water depths and

377   different stage of wave development are shown. At each wave development stage, the

378   percentage taking place under the breaking condition increases as the water depth decreases.

379   At a given water depth, the breaking effect is more prominent at younger wave age but is

380   still important at the equilibrium stage.

381

382
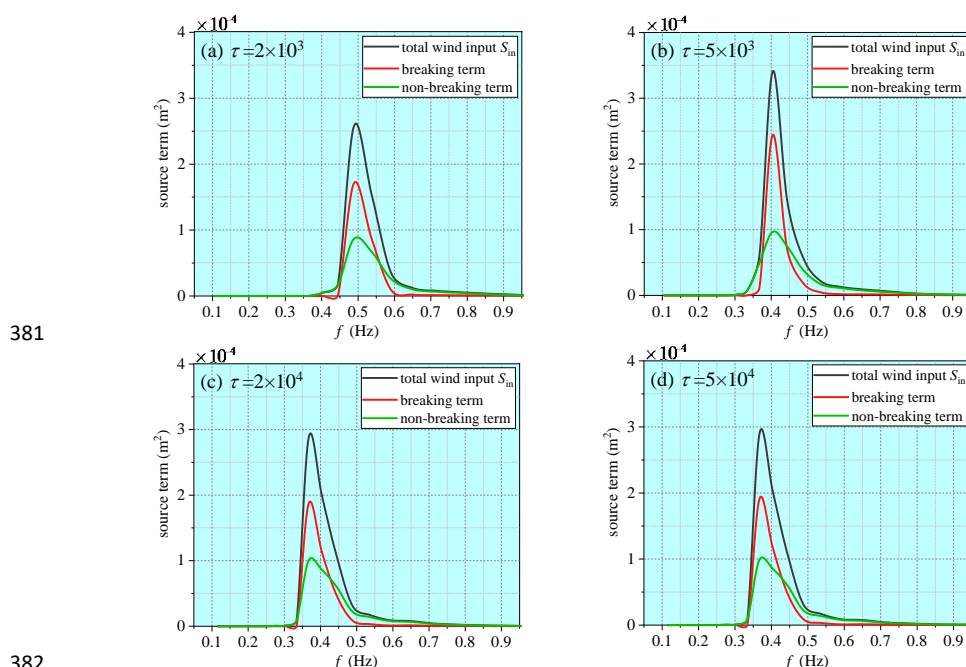
383   Figure 6. Spectra of wind energy input under breaking and non-breaking conditions resulted

384   from the ST-XY source-term package at different wave development stages in a water depth

385   of 2 m
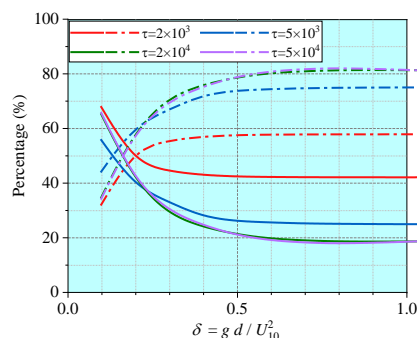
Figure 7. Variations of the percentage for wind energy input under breaking and
non-breaking conditions. Solid lines are those under breaking condition while dot-dash lines
are those under non-breaking condition. Different colors stand for different wave ages.

4. Model Verification under Practical Extreme Conditions

Storm waves under hurricane winds are characterized by the general young wave age
and intensive breaking process, due to the extreme wind speed and rapid-changing wind
directions. Therefore, their modeling requires an accurate description of the wind energy
input to represent such characteristics. In this section, the effectiveness of the ST-XY
source-term option is evaluated. Hurricane Ivan (2004) and Hurricane Katrina (2005), both
of which made landfalls at the coastline of Gulf of Mexico, are chosen for our verification
purpose. Hurricanes Ivan and Katrina are both typical, long-lived, category 4-5 tropical
cyclones with well recorded observational data. In fact, Hurricanes Ivan and Katrina have
been extensively modeled and studied in the literature (Wang et al., 2005; Moon et al., 2008;
Fan et al., 2009; Zieger et al., 2015). In addition, since the tracks of the two hurricanes lie in
the same ocean basin, data of the topography, the forced wind and the ocean currents can be
obtained from the same source, and the model settings can also be kept the same.

4.1 Available data

It is very natural to require possibly most accurate wind data for reliable model results
on ocean wave development (Campos et al., 2018). In this study, we blend the H*wind data
(resulted from the Real-time Hurricane Wind Analysis System operated by the Hurricane
Research Division, National Oceanic and Atmospheric Administration) with the ECMWF
(European Centre for Medium-Range Weather Forecasts) data to build the necessary wind

409   field. The H*wind dataset integrates all field data available during a hurricane event and is

410   usually considered to be highly accurate in a certain range affected by the relevant hurricane

411   (Fan et al., 2009; Liu et al., 2017; Chen and Yu, 2017). The H*wind data is issued every 3 h

412   with a grid resolution of 6 km and a spatial extent of 8°×8° around the hurricane center.

413   Because the H*wind data does not cover the entire simulation domain, the ECMWF data

414   must be supplemented. The ECMWF data has a spatial resolution of 0.125° and temporal

415   resolution of 6 h, which is good enough to represent the background wind field. The wind

416   data from different sources is combined by setting a transition zone so that

417
$$\mathbf{U}_{10} = \begin{cases} \mathbf{U}_{\mathrm{H}} & \left(r < R_{\max}\right) \\ \dfrac{R_{\max} - r}{0.3 R_{\max}} \mathbf{U}_{\mathrm{H}} + \dfrac{r - 0.7 R_{\max}}{0.3 R_{\max}} \mathbf{U}_{\mathrm{E}} & \left(0.7 R_{\max} < r < R_{\max}\right) \\ \mathbf{U}_{\mathrm{E}} & \left(r > R_{\max}\right) \end{cases} \tag{13}$$

418   where, $\mathbf{U}_{\mathrm{H}}$ and $\mathbf{U}_{\mathrm{E}}$ denote the wind velocity vectors from the H*wind dataset and the

419   ECMWF dataset, respectively; r is the distance from the hurricane center; $R_{\max}$ is the

420   maximal distance of the H*wind boundary to the hurricane center. The time interval of the

421   wind field is interpolated to 0.5 h to satisfy the computational condition. The normalized

422   interpolation method of Fan et al. (2009), which ensures the greatest likelihood that the

423   structure of hurricane wind field is not affected by the interpolation, is applied for this

424   purpose. The wind field constructed in such a manner agrees well with the buoy data as

425   shown in Figures 8 and 9. To include the effect of ocean currents (Fan et al., 2009), the

426   global reanalysis database generated with HYCOM (HYbrid Coordinate Ocean Model) and

427   NCODA (Navy Coupled Ocean Data Assimilation) is also utilized as the model input. The

428   data has a spatial resolution of 1/12° and a temporal resolution of 3 h. The topography data

429   is from the ETOPO1 datasets and has a spatial resolution of 1'.

430   Buoy data published by NDBC (National Data Buoy Center, National Oceanic and

431   Atmospheric Administration) are used to validate the model results on representative wave

432   parameters including H_s, T_{02} and spectral wave parameters in both deep- and shallow waters.

433   The locations of buoys are shown in Figure 10.

434
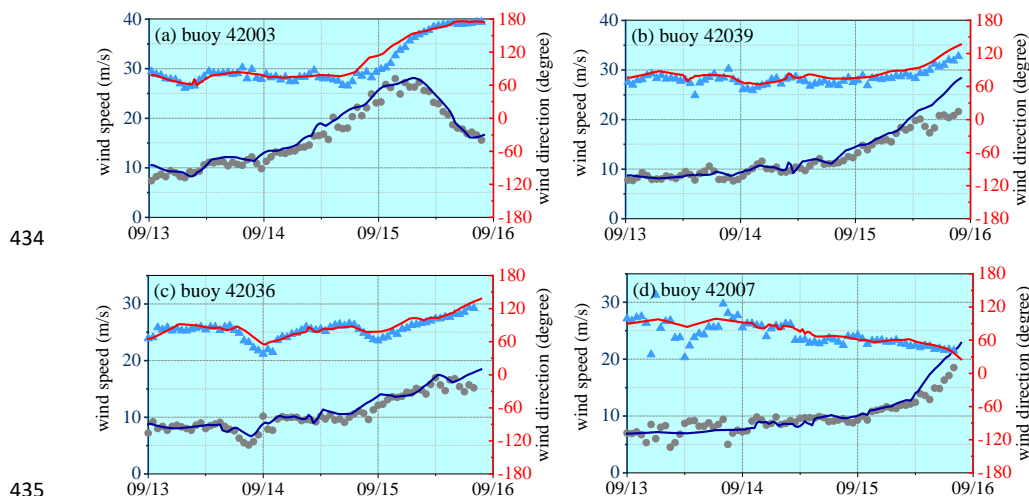
Figure 8. Comparison of reconstructed time series of wind velocity with observed data at

locations of the NDBC buoys during Hurricane Ivan. Scattered dots and triangles are buoy

data of wind speed and wind direction, respectively. Blue and red lines are constructed wind

speed and wind direction, respectively.

441
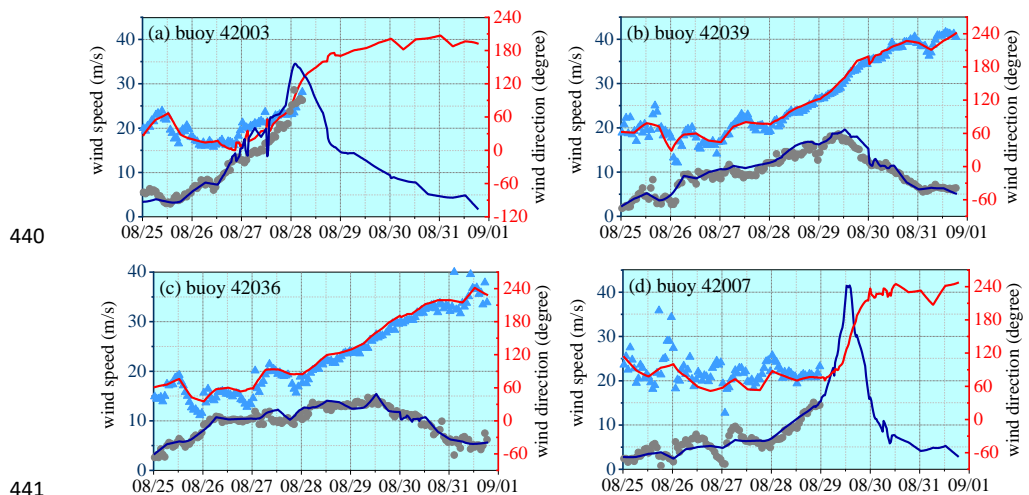
Figure 9. Comparison of reconstructed time series of wind velocity with observed data at

locations of the NDBC buoys during Hurricane Katrina. Scattered dots and triangles are

buoy data of wind speed and wind direction, respectively. Blue and red lines are constructed

wind speed and wind direction, respectively. At buoy 42003 and 42007, there is data

missing.

447 **4.2 Model setup**

448   The computational domain, as shown in Figure 10, covers the area affected by both

449 Hurricane Ivan (2004) and Hurricane Katrina (2005), ranging from 100°W to 82°W and

450 from 18°N to 32°N within Gulf of Mexico. Considering a minimal time period for model

451 warm-up, simulation of Hurricane Ivan is initialized at 00:00 UTC, 12 September 2004 and

452 continues for nearly 4 days until 21:00 UTC, 15 September 2004. Simulation of Hurricane

453 Katrina is initialized at 00:00 UTC, 25 August 2005 and continues for nearly 7 days until

454 18:00 UTC, 31 August 2005. A time step of 10 min is fixed. We assume 36 directional

455 intervals with a constant increment of 10° and 35 frequency intervals that increase

456 logarithmically over the range of 0.0373-1.048 Hz. The numerical results obtained with the

457 ST-XY source-term option are compared to those obtained with other options. The ST2,

458 ST4, ST6 options are implemented with the default setting.
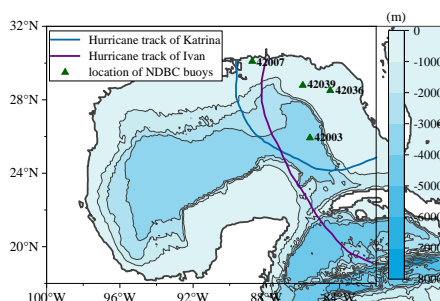
459

460 Figure 10. The computational domain. Tracks of hurricanes are shown with solid lines. The

461 NDBC buoys are marked by triangles. Water depth at the locations of buoys 42003, 42039,

462 42036 and 42007 are 3265 m, 281 m, 50.9 m and 14.9 m, respectively.

463 **4.3 Comparison of wave parameters**

464   The model results on the time variations of the significant wave height H_s and the mean

465 wave period T_{02} at the locations of the buoys during Hurricane Ivan and Hurricane Katrina

466 are shown in Figures 11 and 12, respectively. The observed data are also plotted for

467 comparison. It can be seen that the significant wave height H_s obtained with the ST-XY

468 option agrees fairly well with the buoy data and performs better than the ST2 and ST6

469 options. The peak value and peak time of the significant wave height are accurately

470   represented. In comparison, the significant wave height H_s is obviously overestimated by the

471   ST6 option but underestimated by the ST2 option. The ST4 option performs also very well,

472   but still show some underestimation of the peak values of H_s (as shown in Figures 11a and

473   12a) and some overestimation of H_s before it reaches its maximum value (as shown in

474   Figures 11b-d). The numerical results for the mean wave period T_{02} are shown to be

475   generally less accurate than those for the significant wave height H_s, especially during the

476   period before and after the hurricane event. An underestimation is evident. But, the peak

477   values of T_{02} are still reasonably simulated.
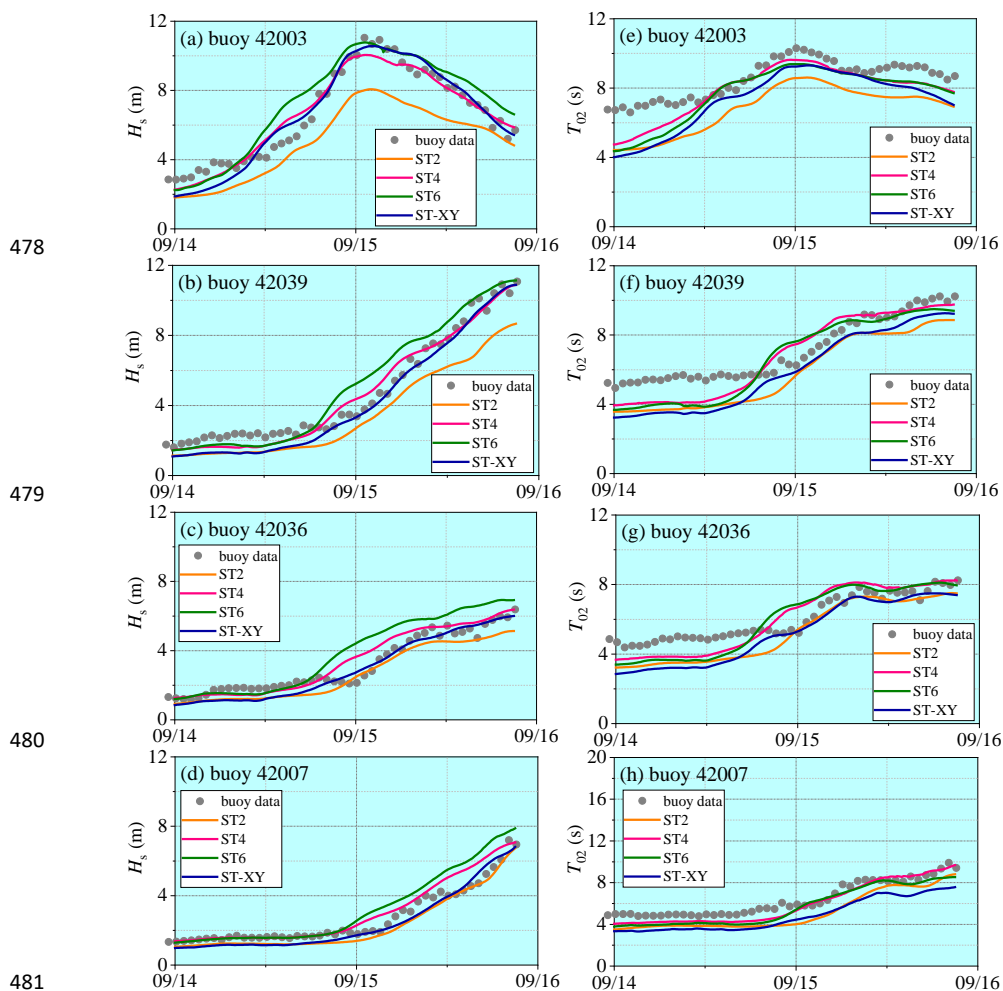
482   Figure 11. Comparisons of the computed variations (lines) of (a) – (d) H_s and (e) – (h) T_{02}

483   with buoy data (dots) during Hurricane Ivan.
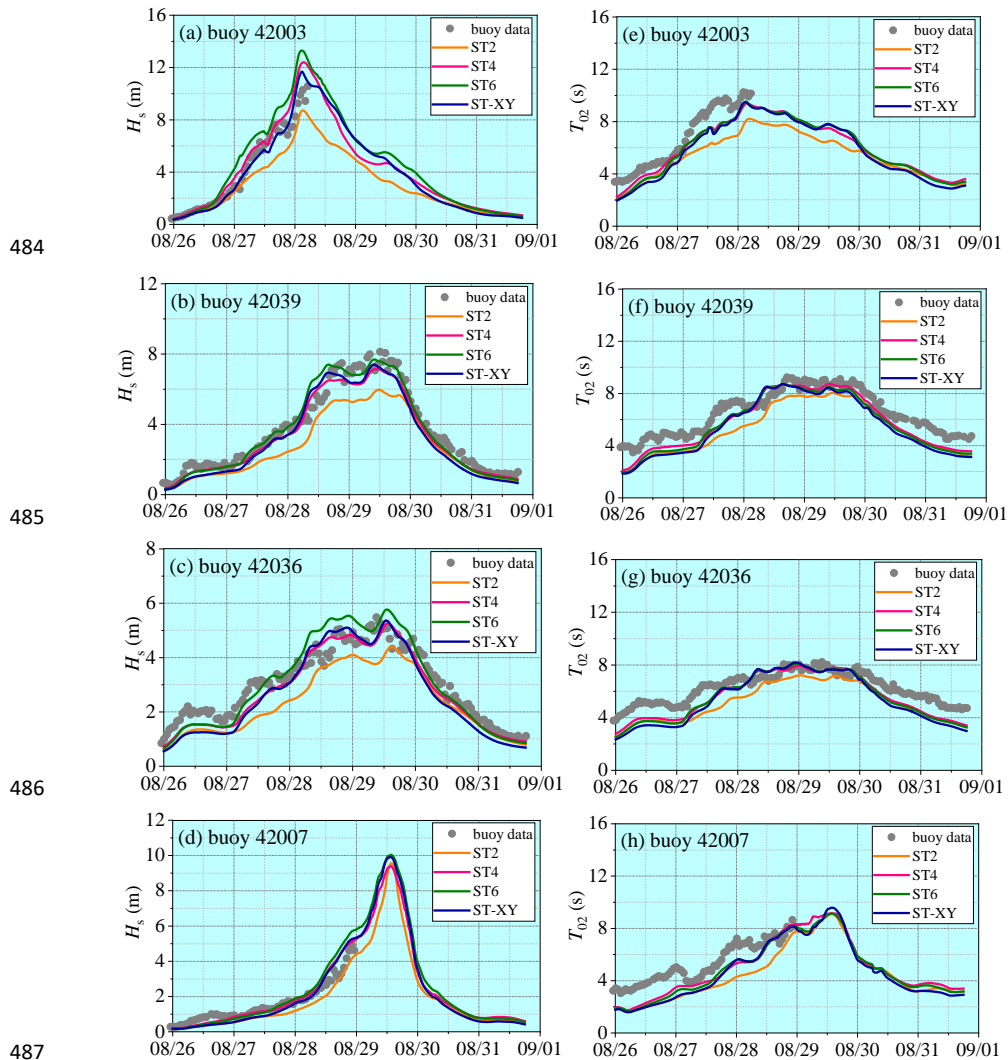
Figure 12. Comparisons of the computed variations (lines) of (a) – (d) H_s and (e) – (h) T_{02}
with buoy data (dots) during Hurricane Katrina.

4.4 Comparison of wave spectra

For the detailed description of a wave spectrum, the peak value E_p, the peak
frequency f_p of the spectrum as well as its mean square slope M_s are defined to describe
the frequency spectrum; the dominant wave propagation direction θ_m, the mean wave
propagation direction $\bar{\theta}$ and the directional spreading width $\Delta\theta$ are defined to describe
the directional spectrum. In particular,

$$E_{\mathrm{p}} = \max\left(\int_0^{2\pi} E\left(f,\theta\right) d\theta\right) \tag{14}$$

$$M_{\mathrm{s}} = \iint k^2 E\left(f,\theta\right) df d\theta \tag{15}$$

$$E\left(\theta_{\mathrm{m}}\right) = \max\left(\int E\left(f,\theta\right) df\right) \tag{16}$$

$$E\left(\theta_{\mathrm{e}}\right) \geq 0.1 \max\left(\int E\left(f,\theta\right) df\right) \tag{17}$$

$$\overline{\theta} = \frac{1}{2}\left(\theta_{\mathrm{e1}} + \theta_{\mathrm{e2}}\right) \tag{18}$$

$$\Delta\theta = \theta_{\mathrm{e2}} - \theta_{\mathrm{e1}} \tag{19}$$

where, E_{p} is the peak value of the frequency spectrum, f_{p} is the corresponding peak frequency; M_{s} is the mean square slope of frequency spectrum, representing the effect of high-frequency wave components; $E\left(\theta_{\mathrm{m}}\right)$ is the peak of the directional spectrum and θ_{m} is the corresponding direction, called the main wave direction; θ_{e} is called the efficient wave direction beyond which the wave energy is below 10% of the peak value of the directional spectrum; θ_{e1} and θ_{e2} are the lower and higher limits of θ_{e}; $\overline{\theta}$ is the mean wave propagation direction while $\Delta\theta$ is the directional range of the effective wave propagation.

Comparison of the computed wave spectra with observations is made at the locations of buoys 42039 and 42036, where a relatively complete data series have been recorded during both hurricane events. Variations of the spectral wave parameters in the deep-water condition (at buoy 42039) are presented in Figures 13 and 14 while those in the shallow water condition (at buoy 42036) are presented in Figures 15 and 16. Accuracy of the numerical results for the peak spectrum value E_{p} is quite similar to that for the representative wave parameters such as H_{s}. The result obtained with the ST-XY option can catch the extreme wave energy condition very well, while the ST6 option always overestimate and the ST2 option underestimate it. The result obtained with the ST4 option overestimates E_{p} under the moderate wind conditions before the extreme events. The numerical results for the peak frequency f_{p} agrees with observations well during both

521   hurricane events. M_s is also satisfactorily simulated, which means that the high frequency

522   part of the wave spectrum is well described by the numerical model. It may be necessary to

523   point out that, different from the results for the representative wave parameters, the peak of

524   E_p may not be correctly represented by any package of the source terms under our

525   consideration in some cases, as shown in Figure 14a.
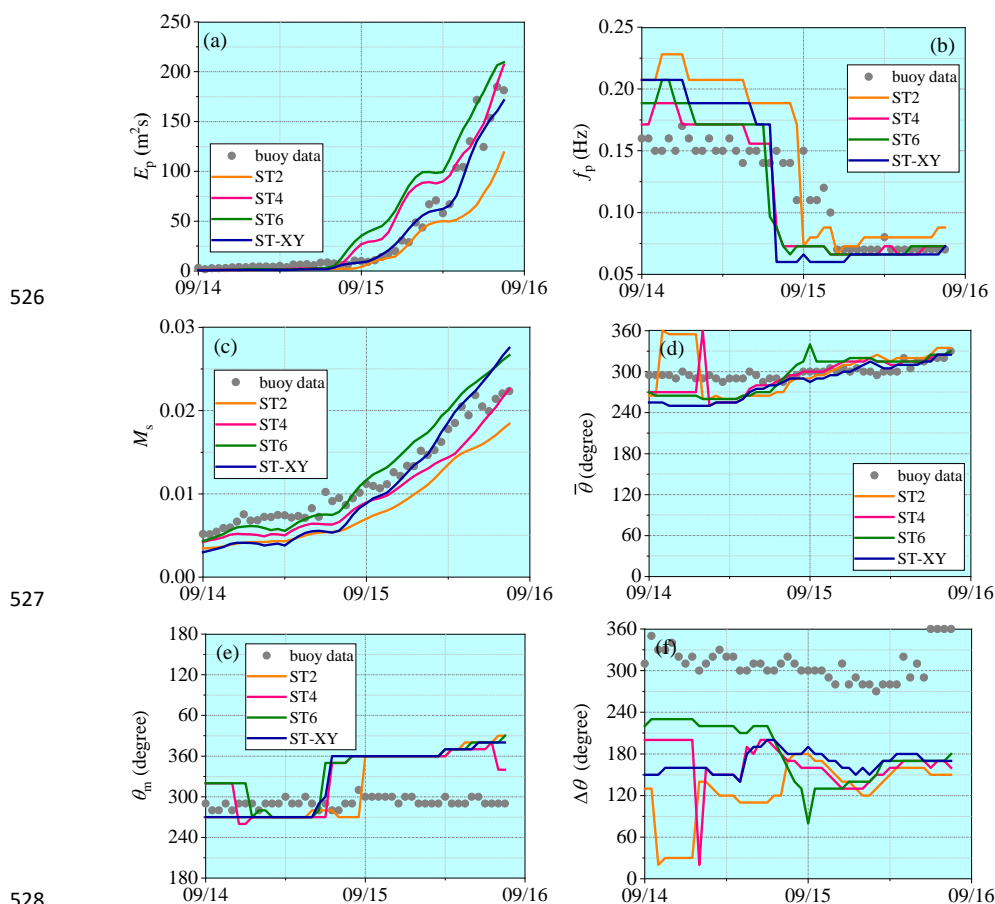
529   Figure 13. Comparisons of wave spectral parameters with observations at buoy 42039

530   during Hurricane Ivan. (a) spectrum peak value; (b) peak frequency; (c) mean square slope;

531   (d) mean wave propagation direction; (e) main wave propagation direction; (f) wave

532   propagation spread width.
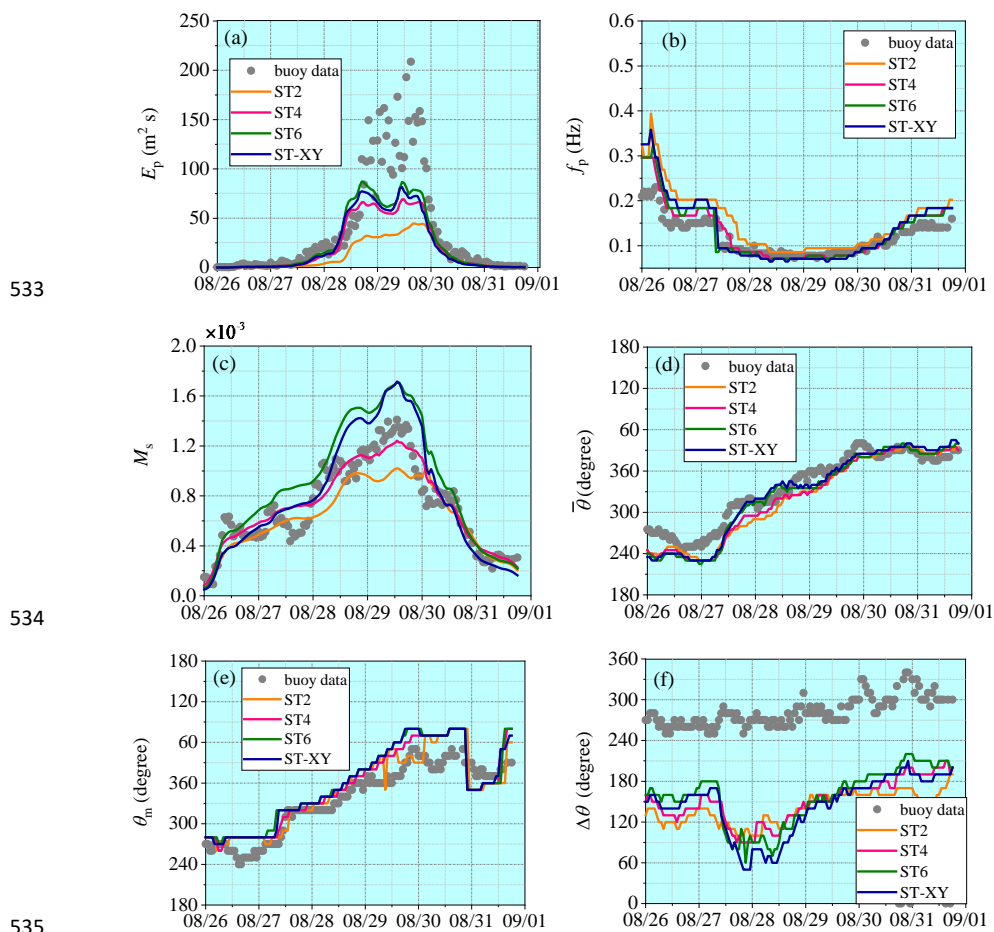
Figure 14. Comparisons of wave spectral parameters with observations at buoy 42039 during Hurricane Katrina. (a) spectrum peak value; (b) peak frequency; (c) mean square slope; (d) mean wave propagation direction; (e) main wave propagation direction; (f) wave propagation spread width.
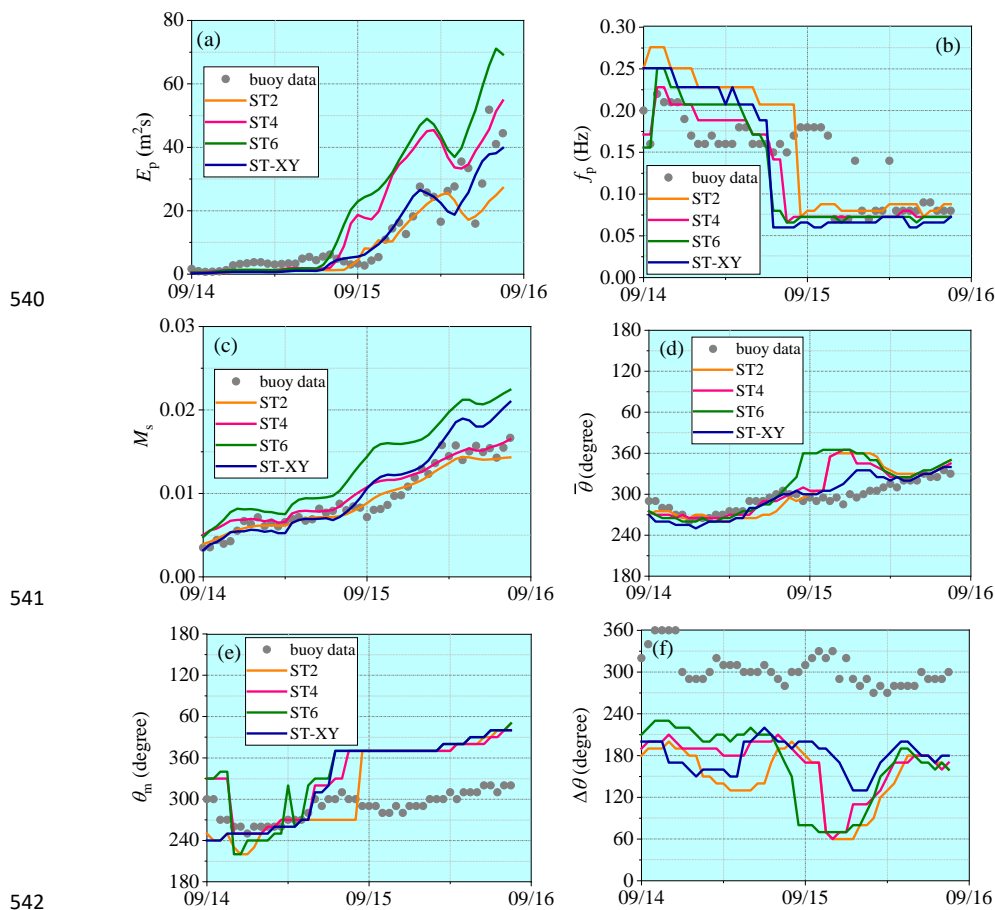
Figure 15. Comparisons of wave spectral parameters with observations at buoy 42036 during Hurricane Ivan. (a) spectrum peak value; (b) peak frequency; (c) mean square slope; (d) mean wave propagation direction; (e) main wave propagation direction; (f) wave propagation spread width.

547

548

549
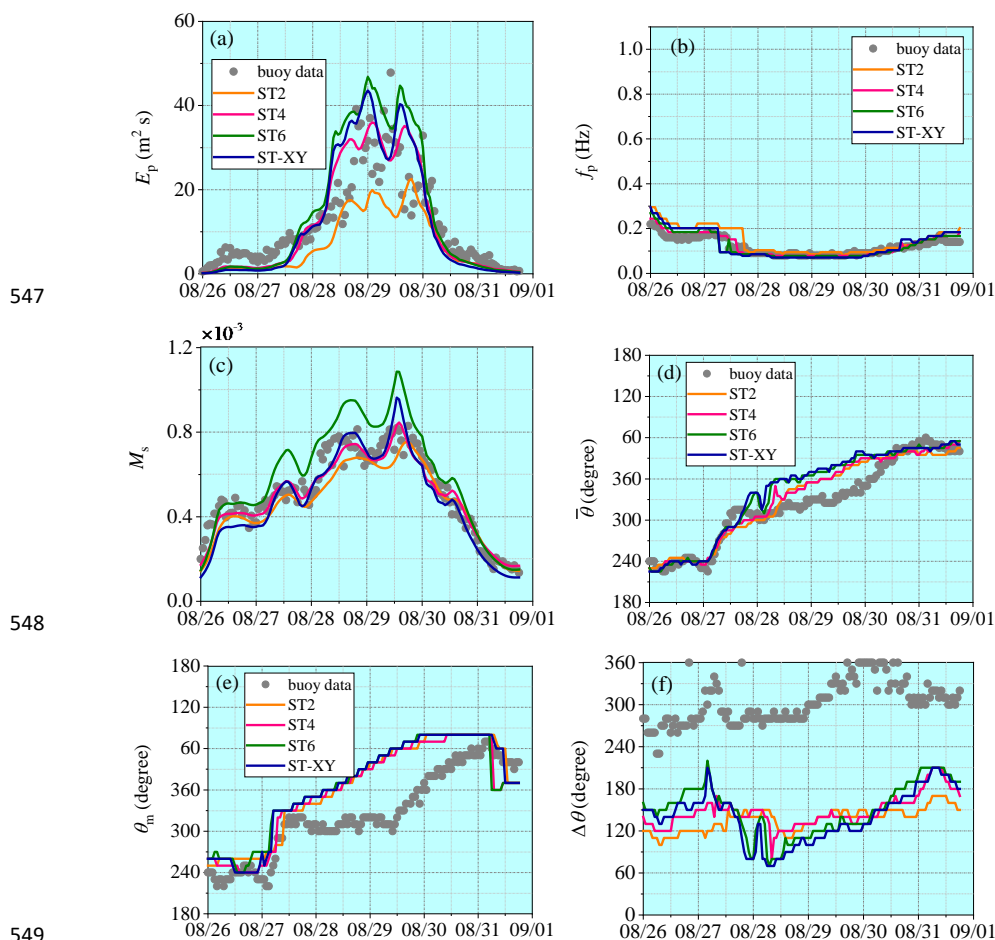
Figure 16. Comparisons of wave spectral parameters with observations at buoy 42036 during Hurricane Katrina. (a) spectrum peak value; (b) peak frequency; (c) mean square slope; (d) mean wave propagation direction; (e) main wave propagation direction; (f) wave propagation spread width.

It is also demonstrated that the numerical results for the main wave propagation direction and the mean wave propagation direction obtained with the ST-XY option and other source-term options are all equally good. However, the numerical result for the directional range of the effective wave propagation is obvious narrower than observed one. This, however, may not be an error of the numerical model since the directional range of the effective wave propagation depends significantly on the methods employed (Earle et al.,

560 1999; Kim et al., 1995). In this study, Longuet-Higgins' method (Longuet-Higgins et al.,

561 1963) is used to build the directional wave spectrum from observed data. This method

562 always leads a broader directional spectrum than other methods with the same parameters

563 (Earle et al. (1999)'s Figure 2).

5. Conclusion

565   This study is aimed to evaluate the performance of the improved formulas for the wind

566 energy input and the wave energy dissipation, i.e., the ST-XY source-term option. The

567 numerical results are obtained with the coupled AWBLM-WWIII model. Both

568 duration-limited waves under idealized conditions and hurricane-generated waves, in both

569 deep and shallow waters are studied. The standard source-term packages of ST2, ST4 and

570 ST6 embedded in WWIII are chosen for comparison. Detailed comparisons are made for not

571 only the representative wave parameters, including the significant wave height, the mean

572 wavelength and the mean wave period, but also the characteristic parameters for the

573 frequency spectrum and the directional spreading function. The effect of breaking on ocean

574 wave modeling is fully discussed.

575   The numerical results show that the ST-XY source-term package performs better than

576 other standard options in general. At the early wave-development stage, the ST-XY option

577 leads to a better agreement of the computed wave energy with the empirical results while

578 other source-term options all tend to underestimate the wave energy. At the equilibrium

579 stage, the results obtained with the ST-XY option approaches the Pierson-Moskowitz limit

580 while ST2 option significantly underestimates the wave energy. The ST-XY option is also

581 effective for ocean wave modeling under both deep- and shallow- water conditions and

582 gives results in good agreement with field data. For hurricane-generated waves, model

583 results obtained with the ST-XY option agrees well with the buoy data and are obviously

584 better than those obtained with other source-term options. On the other hand, the ST6 option

585 often overestimates wave energy while ST2 option leads to an obvious underestimation. The

586 ST4 option performs fairly well but still show some underestimation of the peak value of

587 significant wave height and some overestimation of the significant wave height before its

588 peak value is achieved.

589 Wave breaking significantly affect ocean wave modeling, especially at younger wave

590 ages and in shallower waters. At the early wave-development stage, a significant part of the

591 peak wind energy input takes place under breaking condition, and the proportion decreases

592 gradually as the wave development continues. In shallow waters, the peak value of wind

593 energy input taking place under breaking conditions are always higher than that under

594 non-breaking conditions throughout the early wave-development stage to the equilibrium

595 stage.

596 In summary, the improved formula of Xu and Yu (2020), which includes both breaking

597 effect and the effect of air-flow separation on the leesides of steep wave crests in a

598 consistent way, has a satisfactory performance within the coupled AWBLM-WWIII model.

599 It is physics-based and is verified to be effective for ocean wave modeling under both

600 moderate and extreme wind conditions, at all wave-development stages, and in deep to

601 shallow waters, thus has a broad applicability.

Competing interests

603 The authors declare that there is no conflict of interest.

Authors' contributions

605 Y. Xu and X. Yu conceived of the presented idea. Y. Xu performed the computations. X.

606 Yu supervised the project. Both authors discussed the results and contributed to the final

607 manuscript.

Funding

609 This research is supported by National Natural Science Foundation of China (NSFC)

610 under grant No. 11732008.

Code Availability

612 The code used in this work can be found at https://doi.org/10.5281/zenodo.7047221 (Xu

613 and Yu, 2022a). The input files of the controlled normal-condition cases can be found at

614   https://doi.org/10.5281/zenodo.7047234 (Xu and Yu, 2022b). The input files of hurricane

615   Ivan case can be found at https://doi.org/10.5281/zenodo.7047240 (Xu and Yu, 2022c). The

616   input files of hurricane Katrina case can be found at https://doi.org/10.5281/zenodo.7047244

617   (Xu and Yu, 2022d).

618   **Data Availability**

619   The H*wind data are available at https://www.rms.com/event-response/hwind. The

620   ECMWF-ERA5 wind data are available upon request to https://www.ecmwf.int/. The

621   topography data are available at https://www.ngdc.noaa.gov/mgg/global/global.html. The

622   buoy data can be obtained from NOAA at https://www.ndbc.noaa.gov/.

623   **References**

624   Ardhuin, F., Rogers, E., Babanin, A. V., Filipot, J. F., Magne, R., Roland, A., et al. (2010).

625   Semiempirical dissipation source functions for ocean waves. Part I. definition,

626   calibration, and validation. Journal of Physical Oceanography, 40(9): 1917-1941.

627   Babanin, A. V. and Young, I. R. (2005). Two-phase behaviour of the spectral dissipation of

628   wind waves. Proceedings of the 5th International Symposium on Ocean Waves

629   Measurement and Analysis, Madrid, Spain, Paper No. 51.

630   Babanin, A. V., Banner, M. L., Young, I. R., and Donelan, M. A. (2007). Wave-follower

631   field measurements of the wind-input spectral function. Part III: Parameterization of

632   the wind-input enhancement due to wave breaking. Journal of Physical Oceanography,

633   37(11), 2764-2775.

634   Badulin, S. I., Babanin, A. V., Zakharov, V. E., and Resio, D. (2007). Weakly turbulent laws

635   of wind-wave growth. Journal of Fluid Mechanics, 591: 339-378.

636   Banner, M. L., and Melville, W. K. (1976). On the separation of air flow over water waves.

637   Journal of fluid mechanics, 77(4), 825-842.

638   Battjes, J. A., and Janssen, J. P. F. M. (1978). Energy loss and set-up due to breaking of

639   random waves. In Coastal engineering 1978 (pp. 569-587).

640   Beyá, J., Álvarez, M., Gallardo, A., Hidalgo, H., and Winckler, P. (2017). Generation and

641 validation of the Chilean Wave Atlas database. Ocean Modelling, 116, 16-32.

642 Campos, R. M., Alves, J. H. G. M., Soares, C. G., Guimaraes, L. G., and Parente, C. E.

643  (2018). Extreme wind-wave modeling and analysis in the south Atlantic ocean. Ocean

644  Modelling, 124, 75-93.

645 Cavaleri, L., Alves, J. H., Ardhuin, F., Babanin, A., Banner, M., Belibassakis, K., ... and

646  WISE Group. (2007). Wave modelling–the state of the art. Progress in oceanography,

647  75(4), 603-674.

648 Cavaleri, L., Barbariol, F., and Benetazzo, A. (2020). Wind–wave modeling: Where we are,

649  where to Go. Journal of Marine Science and Engineering, 8(4), 260.

650 CERC (1977). Shore protection manual. U.S. Army Coastal Research Center, Vols. 1–3.

651 Chalikov, D. (1995). The parameterization of the wave boundary layer. Journal of Physical

652  Oceanography, 25(6), 1333-1349.

653 Chalikov, D. V., and Belevich, M. Y. (1993). One-dimensional theory of the wave boundary

654  layer. Boundary-Layer Meteorology, 63(1-2), 65-96.

655 Chen, Y. and Yu, X. (2017). Sensitivity of storm wave modeling to wind stress evaluation

656  methods. Journal of Advances in Modelling Earth System, 9: 893-907.

657 Csanady, G. T. (2001). Air-Sea Interaction: Laws and Mechanisms. Cambridge University

658  Press, New York.

659 Donelan, M. A., and Pierson Jr, W. J. (1987). Radar scattering and equilibrium ranges in

660  wind-generated waves with application to scatterometry. Journal of Geophysical

661  Research: Oceans, 92(C5): 4971-5029.

662 Donelan, M. A., Babanin, A. V., Young, I. R., and Banner, M. L. (2006). Wave-follower

663  field measurements of the wind-input spectral function. Part II: Parameterization of the

664  wind input. Journal of physical oceanography, 36(8): 1672-1689.

665 Donelan, M.A., (2001). A nonlinear dissipation function due to wave breaking. Proceedings

666  of ECMWF Workshop on Ocean Wave Forecasting, 87–94, ECMWF, Reading, U.K.

667 Earle, M. D., Steele, K. E., and Wang, D. W. C. (1999). Use of advanced directional wave

668  spectra analysis methods. Ocean engineering, 26(12), 1421-1434.

669 Eldeberky, Y. (1996). Nonlinear transformationations of wave spectra in the nearshore zone.

670   Unpublished doctoral dissertation, Delft University of Technology, Delft, The
671   Netherlands.

672 Fan, Y., and Rogers, W. E. (2016). Drag coefficient comparisons between observed and
673   model simulated directional wave spectra under hurricane conditions. Ocean Modelling,
674   102, 1-13.

675 Fan, Y., Ginis, I., Hara, T., Wright, C. W., and Walsh, E. J. (2009). Numerical simulations
676   and observations of surface wave fields under an extreme tropical cyclone. Journal of
677   Physical Oceanography, 39(9), 2097-2116.

678 Hasselmann, K. (1974). On the spectral dissipation of ocean waves due to white capping.
679   Boundary-Layer Meteorology, 6(1-2): 107-127.

680 Hasselmann, K., Barnett, T. P., Bouws, E., Carlson, H., Cartwright, D. E., Enke, K. et al.
681   (1973). Measurements of wind-wave growth and swell decay during the Joint North
682   Sea Wave Project (JONSWAP). Ergänzungsheft, 8-12.

683 Hwang, P. A. (2005). Temporal and spatial variation of the drag coefficient of a developing
684   sea under steady wind-forcing. Journal of Geophysical Research: Oceans, 110(C7).

685 Hwang, P. A., and Wang, D. W. (2004). An empirical investigation of source term balance of
686   small scale surface waves. Geophysical research letters, 31(15).

687 Janssen, P. A. E. M. (1989). Wave-induced stress and the drag of air flow over sea waves.
688   Journal of Physical Oceanography, 19(6): 745-772.

689 Janssen, P. A. E. M. (1991). Quasi-linear theory of wind-wave generation applied to wave
690   forecasting. Journal of Physical Oceanography, 21(21): 1631-1642.

691 Janssen, P. A. E. M. (2004), The Interaction of Ocean Waves and Wind. Cambridge
692   University Press, Cambridge, U.K.

693 Jones, I. S. and Toba, Y. (2001). Wind Stress over the Ocean. Cambridge University Press,
694   New York.

695 Kahma, K. K., and Calkoen, C. J. (1992). Reconciling discrepancies in the observed growth
696   of wind-generated waves. Journal of Physical Oceanography, 22(12), 1389-1405.

697 Kim, T., Lin, L. H., and Wang, H. (1995). Application of maximum entropy method to the
698   real sea data. In Coastal Engineering 1994 (pp. 340-355).

699 Leckler, F., Ardhuin, F., Filipot, J. F., and Mironov, A. (2013). Dissipation source terms and
700   whitecap statistics. Ocean Modelling, 70: 62-74.

701 Liu, Q., Babanin, A., Fan, Y., Zieger, S., Guan, C., and Moon, I. J. (2017). Numerical
702   simulations of ocean surface waves under hurricane conditions: Assessment of existing
703   model performance. Ocean Modelling, 118, 73-93.

704 Longuet-Higgins, M. S. (1969). On wave breaking and the equilibrium spectrum of
705   wind-generated waves. Proceedings of the Royal Society of London. A. Mathematical
706   and Physical Sciences, 310(1501), 151-159.

707 Longuet-Higgins, M. S., Cartwright, D. E., and Smith, N. D. (1963). "Observations of the
708   Directional Spectrum of Sea Waves Using The Motion of a Floating Buoy", in Ocean
709   Wave Spectra, Prentice Hall, Englewood Cliffs, N. J., pp.111-136.

710 Makin, V. K., and Kudryavtsev, V. N. (1999). Coupled sea surface-atmosphere model: 1.
711   Wind over waves coupling. Journal of Geophysical Research: Oceans, 104(C4),
712   7613-7623.

713 Melville, W. K. and Matusov, P. (2002). Distribution of breaking waves at the ocean surface.
714   Nature, 417: 58.

715 Mentaschi, L., Besio, G., Cassola, F., and Mazzino, A. (2015). Performance evaluation of
716   Wavewatch III in the Mediterranean Sea. Ocean Modelling, 90, 82-94.

717 Miles, J. W. (1957). On the generation of surface waves by shear flows. Journal of Fluid
718   Mechanics, 3(2): 185-204.

719 Miles, J. W. (1965). A note on the interaction between surface waves and wind profiles.
720   Journal of Fluid Mechanics, 22(4): 823-827.

721 Moon, I. J., Ginis, I., and Hara, T. (2008). Impact of the reduced drag coefficient on ocean
722   wave modeling under hurricane conditions. Monthly Weather Review, 136(3),
723   1217-1223.

724 Moskowitz, L. (1964). Estimates of the power spectrums for fully developed seas for wind
725   speeds of 20 to 40 knots. Journal of geophysical research, 69(24), 5161-5179.

726 Phillips, O. M. (1985). Spectral and statistical properties of the equilibrium range in
727   wind-generated gravity waves. Journal of Fluid Mechanics, 156: 505-531.

728 Phillips, O. M., Posner, F. L., and Hansen, J. P. (2001). High range resolution radar
729   measurements of the speed distribution of breaking events in wind-generated ocean
730   waves: surface impulse and wave energy dissipation rates. Journal of Physical
731   Oceanography, 31: 450-460.

732 Pierson Jr, W. J., and Moskowitz, L. (1964). A proposed spectral form for fully developed
733   wind seas based on the similarity theory of SA Kitaigorodskii. Journal of geophysical
734   research, 69(24), 5181-5190.

735 Polnikov, V. G., (1993). On a description of a wind–wave energy dissipation function. In:
736   Donelan, M. A., Hui, W. H., Plant, W. J. (Eds.), The Air–sea Interface. Radio and
737   Acoustic Sensing, Turbulence and Wave Dynamics. Rosenstiel School of Marine and
738   Atmospheric Science, University of Miami, Miami, FL, 277-282.

739 Rogers, W. E., Babanin, A. V., and Wang, D. W. (2012). Observation-consistent input and
740   whitecapping dissipation in a model for wind-generated surface waves: Description
741   and simple calculations. Journal of Atmospheric and Oceanic Technology, 29(9),
742   1329-1346.

743 Sanders, J. W. (1976). A growth-stage scaling model for the wind-driven sea. Deutsche
744   Hydrografische Zeitschrift, 29(4), 136-161.

745 Snyder, R. L., Dobson, F. W., Elliott, J. A., and Long, R. B. (1981). Array measurements of
746   atmospheric pressure fluctuations above surface gravity waves. Journal of Fluid
747   mechanics, 102: 1-59.

748 Stewart, R. W. (1961). The wave drag of wind over water. Journal of fluid mechanics, 10(2),
749   189-194.

750 Stopa, J. E., Ardhuin, F., Babanin, A., and Zieger, S. (2016). Comparison and validation of
751   physical wave parameterizations in spectral wave models. Ocean Modelling, 103, 2-17.

752 The WAVEWATCH III R Development Group (WW3DG) (2016). User manual and system
753   documentation of WAVEWATCH III R version 5.16. Tech. Note 329,
754   NOAA/NWS/NCEP/MMAB, College Park, MD, USA, 326 pp. + Appendices.

755 Tolman, H. L. (2002). Validation of WAVEWATCH III version 1.15 for a global domain.
756   Technical Note, 213, 33.

757 Tolman, H. L., and Chalikov, D. (1996). Source terms in a third-generation wind wave
758   model. Journal of Physical Oceanography, 26(11), 2497-2518.

759 Wang, D. W., Mitchell, D. A., Teague, W. J., Jarosz, E., and Hulbert, M. S. (2005). Extreme
760   waves under hurricane Ivan. Science, 309(5736), 896-896.

761 Xu, Y., and Yu, X. (2020). Enhanced formulation of wind energy input into waves in
762   developing sea. Progress in Oceanography, 186, 102376.

763 Xu, Y., and Yu, X. (2021). Enhanced atmospheric wave boundary layer model for evaluation
764   of wind stress over waters of finite depth. Progress in Oceanography, 198, 102664.

765 Xu, Y., and Yu, X. (2022a): Enhanced Ocean Wave Modeling by Including Effect of
766   Breaking under Both Deep- and Shallow-Water Conditions – code files, Zenodo,
767   https://doi.org/10.5281/zenodo.7047221.

768 Xu, Y., and Yu, X. (2022b): Enhanced Ocean Wave Modeling by Including Effect of
769   Breaking under Both Deep- and Shallow-Water Conditions – input files of the
770   controlled normal condition cases, Zenodo, https://doi.org/10.5281/zenodo.7047234.

771 Xu, Y., and Yu, X. (2022c): Enhanced Ocean Wave Modeling by Including Effect of
772   Breaking under Both Deep- and Shallow-Water Conditions – input files of hurricane
773   Ivan case, Zenodo, https://doi.org/10.5281/zenodo.7047240.

774 Xu, Y., and Yu, X. (2022d): Enhanced Ocean Wave Modeling by Including Effect of
775   Breaking under Both Deep- and Shallow-Water Conditions – input files of hurricane
776   Katrina case, Zenodo, https://doi.org/10.5281/zenodo.7047244.

777 Young, I. R. (1999). Wind generated ocean waves. Elsevier.

778 Young, I. R., and Verhagen, L. A. (1996). The growth of fetch limited waves in water of
779   finite depth. Part 1. Total energy and peak frequency. Coastal Engineering, 29(1-2),
780   47-78.

781 Yuan, Y., Tung, C. C., and Huang, N. E. (1986). Statistical characteristics of breaking waves.
782   In: Phillips, O. M., Hasselmann, K. (Eds.), Wave Dynamics and Radio Probing of the
783   Ocean Surface. Plenum Press, New York, 265-272.

784 Zakharov, V. E., Resio, D., and Pushkarev, A. (2012). New wind input term consistent with
785   experimental, theoretical and numerical considerations. arXiv preprint

786   arXiv:1212.1069.

787   Zakharov, V., Resio, D., and Pushkarev, A. (2017). Balanced source terms for wave

788   generation within the Hasselmann equation. Nonlinear Processes in Geophysics, 24(4),

789   581-597.

790   Zieger, S., Babanin, A. V., Rogers, W. E., and Young, I. R. (2015). Observation-based source

791   terms in the third-generation wave model WAVEWATCH. Ocean Modelling, 96, 2-25.

792